

In-situ Measurements for Snow Grain Size and Shape Characterization Using Optical Methods

B. MONTPETIT¹, A. ROYER¹, A. LANGLOIS¹, M. CHUM¹, P. CLICHE¹, A. ROY¹, N. CHAMPOLLION², G. PICARD², F. DOMINÉ², AND R. OBBARD³

ABSTRACT

The snow grain size and shape characterization, their evolution in depth (stratigraphy) and through the winter (metamorphism) are key parameters for the improvement and validation of climate and radiative transfer models as well as for remote sensing retrieval methods. This paper describes and discusses four different optical methods (two active and two passive shortwave methods) for *in-situ* determination of the specific surface area (SSA) of snow grains. We present a new shortwave infrared (SWIR) camera approach, compared with a light SWIR laser-based system measuring snow albedo through an integrating sphere (InfraRed Integrating Sphere, IRIS), similar to the system previously proposed by Gallet et al. (2009). The SWIR camera approach shows improved sensitivity to snow SSA when compared to the near-infrared camera, given a more contrasted and better calibrated image of the snow stratigraphy in a snowpit. The IRIS measurements directly on the wall of the snowpit, i.e. without snow sample extraction, give a better vertical resolution of measurements, but with a higher uncertainty than measurements based on extracted snow samples (fixed method). Improved accuracy (10%) and reproducibility in SSA measurements are obtained using the fixed IRIS system on extracted samples, validated against several methane (CH_4) adsorption and X-ray computed micro-tomography measurements. Complementary to these measurements, macro-photographs of individual snow grains with an innovative multi-directional diode lighting system were taken. This method is very easy to handle in the field and allowing the retrieval of three dimensional (3D) representations of the snow grains. Such 3D snow grain representation appears very useful to characterize the snow grain shapes and types of extracted snow samples at each snowpack layers.

Keywords: Specific Surface Area, Albedo, Snow grain size, Snow grain shape

INTRODUCTION

The snowpack parameterization (depth, density, wetness, temperature, cohesion and snow grain size/shape) is important for many climate and hydrological applications (surface energy balance, avalanche predictions, water resources management) (e.g. Hall, 2004; Armstrong and Brun, 2008; Brown, 2010; Foster et al., 2011). The seasonal and vertical snow grain size characterization are key parameters for snow albedo retrieval from solar satellite data (Jin et. al., 2008; Lyapustin et al., 2009; Fernandes et al., 2009), for snow water equivalent retrieval from microwave satellite

¹ Centre d'Applications et de Recherches en Télédétection, Université de Sherbrooke, Québec, Canada.

² Université Joseph Fourier - Grenoble 1 / CNRS, Laboratoire de Glaciologie et Géophysique de l'Environnement, France.

³ Thayer School of Engineering, Dartmouth College, Hanover, NH, USA.

data (e.g. Chang et al., 1982; Durand et. al., 2008; Mätzler, 2006; Pulliainen, 2006; Derksen et al., 2010; Langlois et al., 2010a) and for studies of atmospheric-snow chemistry interactions (Grannas et. al., 2007; Dominé et. al., 2008). These analysis models still need to be improved with reliable and accurate ground-based snow grain measurements.

Here, we present a new SWIR camera approach, at wavelengths comparable to our SWIR integrating sphere system (InfraRed Integrating Sphere, IRIS) and to the DUFISSS (Dual Frequency Intergrating Sphere for Snow Specific surface area) system (Gallet et al., 2009). Compared to the DUFISSS system, our IRIS system has two types of settings: mobile setting, which allows albedo measurements without extracting a snow sample and; fixed setting using extracted sample of snow, similar to the DUFISSS system. In parallel to these measurements, macro-photographs using a new multi-directional lighting system were taken allowing a three dimensional representation of the snow grains.

Greatest extension (diameter, D_{\max}) of snow grain measured in millimeters has long been used as a classical parameter for characterizing its size (Fierz et. al., 2009). Given the variety of grain shapes (precipitation particles, rounded grains, faceted crystals, depth hoar, etc) and size distributions (Fierz et. al., 2009), the definition of grain size remains ambiguous (Aoki et. al. 2000; Mätzler, 2002; Taillandier et. al., 2007) and improved measurements methods are required. Moreover, grains are sometimes not a clear component of a snowpack as the boundaries between them are not always clearly identifiable (Dominé et al., 2008). Hence, the main objective of this paper is to analyze and compare several optically-based field retrieval methods of snow grain size and to discuss their accuracy and reproducibility with various measurements taken in Northern Canada and the French Alps.

MODELED EFFECTS OF GRAINS SIZE AND SHAPE ON SNOW ALBEDO

In radiative transfer studies, the “optical” diameter of particles (D_o) is commonly used to characterize particle sizes for any given shape using the volume (V) to surface area (A) ratio

where $D_o = 6 \frac{V}{A}$ (e.g. Grenfell and Warren, 1999). The optical diameter can also be related to the

so-called specific surface area (SSA) of particles. SSA can be defined by its surface area (A) to

volume (V) ratio ($SSA = \frac{A}{V}$) (in mm^{-1}). The relationship between the optical diameter and the

SSA is then: $D_o = \frac{6}{SSA}$. In this study, we used the simple optical equation model suggested by

Kokhanovsky and Zege (2004) (hereafter referred to as KZ04) for snow albedo computation:

$$R_{a,\lambda} = \exp\left(-K_0 b \sqrt{\gamma_\lambda \left(\frac{6}{SSA}\right)}\right) = \exp\left(-K_0 b \sqrt{\gamma_\lambda D_o}\right) \quad (1)$$

where $R_{a,\lambda}$ is the spectral albedo, at the wavelength λ , γ_λ is the absorption coefficient of ice which depends on the imaginary part of the refraction index of ice (the refraction indexes were taken from Wiscombe, 2005), the constant b represents the shape factor and accounts for various types of grains (b ranges from 4.53 for spheres to 3.62 for tetrahedral grains, see Picard et al., 2009a), D_o is the optical diameter of the snow grain and K_0 is the escape function and depends mainly on the incident lighting conditions ($\frac{7}{7}$ for normal incidence albedo and 1 for plane albedo). Figure1A clearly shows the higher sensitivity of snow albedo to D_o in the SWIR region ($>1.2\mu\text{m}$) compared to the NIR region ($<1.0\mu\text{m}$).

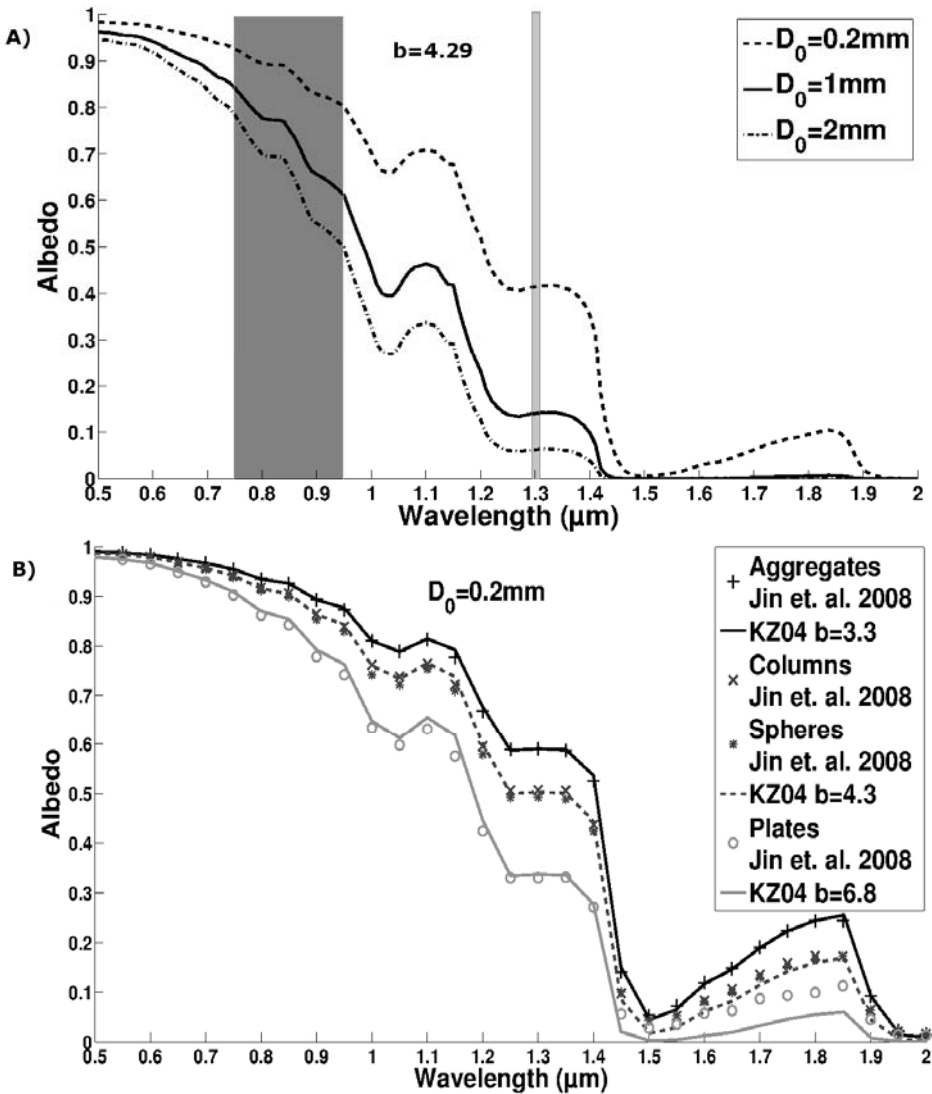


Figure 1. Spectral albedo of snow: A) for different grain sizes (D_0) simulated with the KZ04 model for normal incident lighting ($K_0=9/7$). The spectral responses of the NIR (dark gray rectangle) and SWIR (light gray rectangle) cameras are displayed. The wavelength of the IRIS and DUFISSS laser system are included in the SWIR camera spectral response. B) for different grain shape factors simulated with the KZ04 model for plane albedo ($K_0=1$ and given b valCues) fitted to the Jin et. al. (2008) data (personnal communication).

The effect of the snow grain shape is illustrated in Figure 1. Spectral albedo of snow: A) for different grain sizes (D_0) simulated with the KZ04 model for normal incident lighting ($K_0=9/7$). The spectral responses of the NIR (dark gray rectangle) and SWIR (light gray rectangle) cameras are displayed. The wavelength of the IRIS and DUFISSS laser system are included in the SWIR camera spectral response. B) Simulations from the KZ04 model using different values of b are compared to computed spectral albedo using the improved geometric-optics method (IGOM) developed by Yang and Liou (1996) (derived from the data of Jin et al., 2008, personal communication). Four idealized shapes: aggregates of columns, solid hexagonal columns, spheres and hexagonal plates, were considered. For the same effective equivalent grain size, i.e. the effective diameter D_{eff} defined above, aggregates have the highest albedo, whereas plates have the lowest. Spheres and columns produce similar spectral albedo (Figure 1. Spectral albedo of snow:

A) for different grain sizes (D_o) simulated with the KZ04 model for normal incident lighting ($K_0=9/7$). The spectral responses of the NIR (dark gray rectangle) and SWIR (light gray rectangle) cameras are displayed. The wavelength of the IRIS and DUFISSS laser system are included in the SWIR camera spectral response.B) because they have similar asymmetry factors (Jin et al., 2008). Using an iterative approach to optimize the fit between the KZ04 and Jin et al. models, we sought the value of b which gives the best fit. Results show that b values ranges from 3.3 for aggregates to 4.3 for spheres or columns and 6.8 for plates (Figure 1B). These behaviors of spectral albedo variation (Figure1. Spectral albedo of snow: A) for different grain sizes (D_o) simulated with the KZ04 model for normal incident lighting ($K_0=9/7$). The spectral responses of the NIR (dark gray rectangle) and SWIR (light gray rectangle) cameras are displayed. The wavelength of the IRIS and DUFISSS laser system are included in the SWIR camera spectral response.B) given for mono-dispersed sizes of idealized particles show that the shape of the snow grain could be important in the retrieval procedure, as also outlined by Picard et al. (2009a). However, in practice, snow grain samples include different sizes and shapes giving a poly-dispersed particle distribution. This will be discussed further in the result section.

INSTRUMENTS USED TO DERIVE SSA AND GRAIN SHAPE

NIR and SWIR cameras

One of the instruments used in this study is sensitive to the near infrared and shortwave infrared (0.9-1.7 μm) based on a cooled InGaAs array (320x256 pixels) (© Xenics Xeva-320). A filter centered at $1.295 \pm 0.012 \mu\text{m}$ (Edmund NT62-863) is placed in front of the lens. This wavelength was chosen for the optimum sensitivity of the spectrum albedo to SSA (Figure1A). The advantage of such an instrument is the possibility to directly derive (after calibration) SSA the KZ04 model as shown in the previous section.

We also use a Charged-Coupled Device (CCD) camera to acquire photos in the NIR spectrum, as suggested by Matzl and Schneebeli (2006). The Nikon AS-F D1X with 18-70 mm zoom lens was converted to an infrared camera at 0.75 μm (filter placed in front of the CCD) (see Langlois et al., 2010b).

All measurements are done under diffuse lighting conditions using a white blanket, avoiding direct solar illumination. Following the protocol suggested by Langlois et al. (2010b), we also use image normalization to correct illumination variations over the image by successively taking an image of the snow profile (the snowpit wall) and a large reference homogenous panel nearly lambertian covering the hole surface of the snow wall. Furthermore, for each snow picture, at least two reference targets (Spectralon panels with reflectance values of 0.25 and 0.59 at 1.3 μm) were placed on the snow wall in order to establish the linear albedo relationship between the normalized 16-bit grayscale digital number and the reference albedo. Figure 1 shows the expected linearity and the high sensitivity of the cameras used. Such linear relationships are computed for each snowpit taking into account variations in lighting and geometric conditions. Figure 2 shows an example of a normalized image acquired with the NIR (left) and SWIR (right) cameras. The NIR image shows a better vertical resolution (mm/pixel) but the SWIR image shows a much more detailed snowpit stratigraphy (i.e. more sensitive to changes in SSA and density).

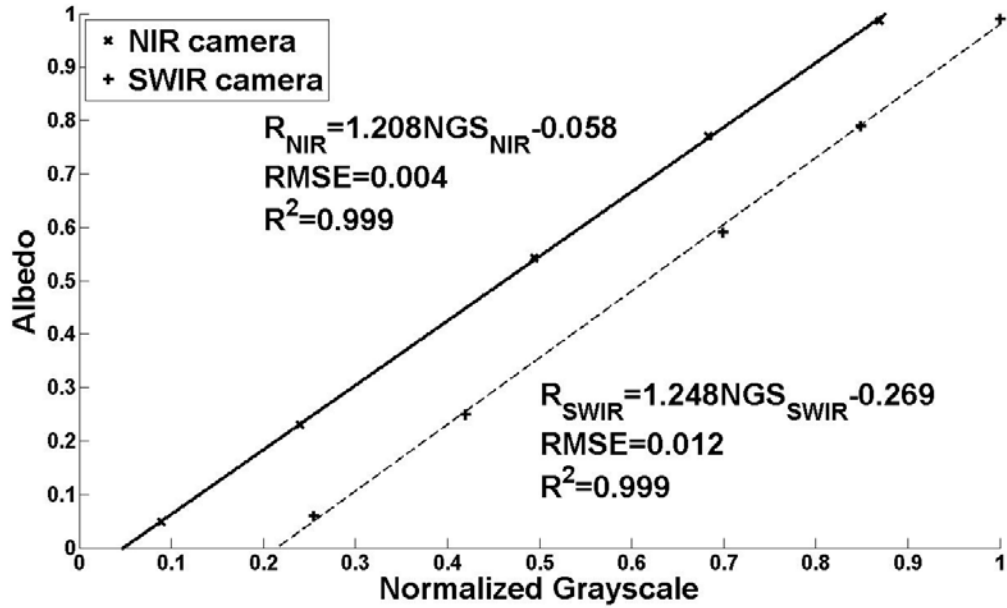


Figure 1. Typical NIR and SWIR albedo calibration curves.

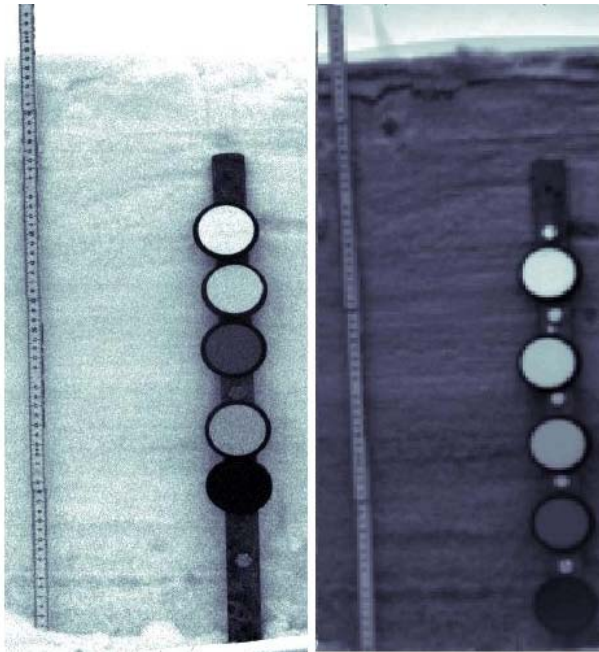


Figure 2. Example of a normalized NIR (left) and SWIR (right) image of the same 1m snowpit taken on the Sherbrooke University campus. Five Spectralon reference targets (nominal reflectances of 5, 20, 50, 75 and 100% from the bottom to the top) can also be seen.

Shortwave InfraRed Integrating Sphere (IRIS) system

Another system used to measure snow albedo is the Shortwave InfraRed Integrating Sphere (IRIS) system, similar to the one developed by Gallet et al. (2009), using an integrating sphere (Labsphere ®, 10cm diameter) with 3 holes. The first hole is for illumination by a $1.3\mu\text{m}$ laser with a 1-cm beam expander. The second hole, in front of the laser, is placed in front of the target (snow sample) and the third one, in the perpendicular plane, is for an InGaAs photodiode detector. A diaphragm is put in front of the laser beam in order to measure the dark current and possible

parasitic light coming into the sphere. This light and simple system allows two operational modes: a fixe mode where a snow sample is extracted (cylinder sampler of 10cm diameter and 6 cm height) and put under the integrating sphere in a fixed position; and a mobile mode where the integrating sphere is placed directly against the snow wall (Figure 3). The mobile mode allows measurements directly on the natural snow surface without destroying its structure by extracting a snow sample. The cylinder used to sample the snow for the fixed mode is sufficiently large and high to avoid errors due to internal reflections of light (Gallet et al., 2009).

As for the NIR and SWIR cameras, the IRIS system is calibrated to albedo for each snowpit using the same reference lambertian Spectralon targets taking into account any possible shift in the laser illumination. Figure 4 shows an example of a calibration curve. The non-linear response is due to a re-illumination effect of the reference panels by their reflected light (the higher the albedo, stronger is the re-illumination).



Figure 3. Mobile IRIS system setup.

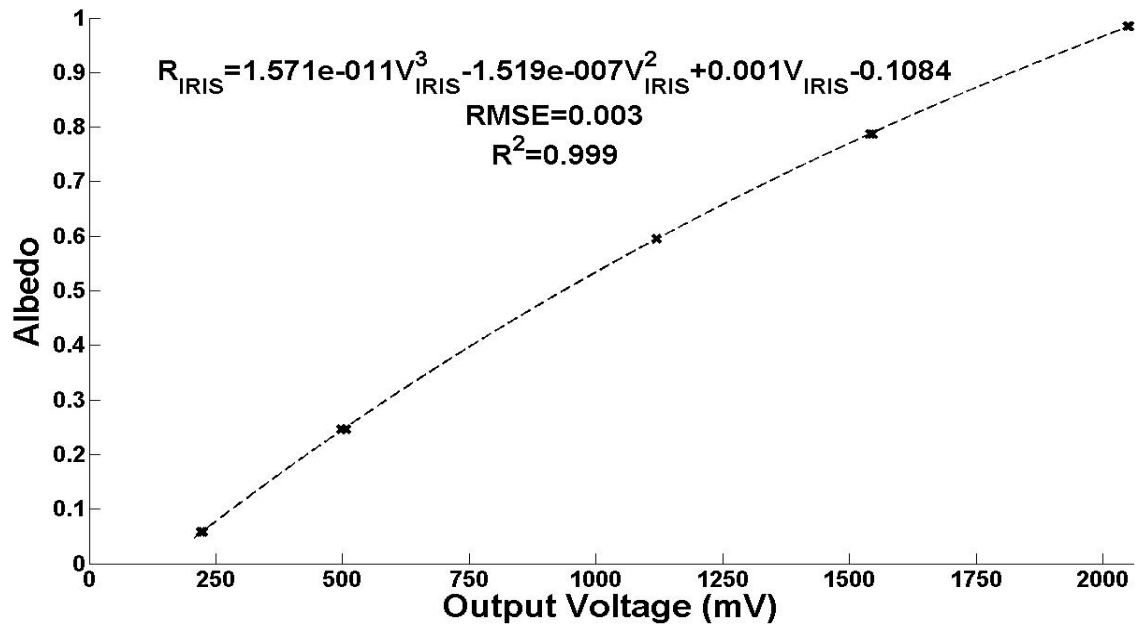


Figure 4. Typical IRIS reflectance calibration curve.

Multidirectional lighting macro-photographs

In order to analyze the shape of the snow grain, we developed a simple optical system that uses, within an enclosed box, five blue diodes illuminating from five directions (nadir, N, E, S and W) a gridded green plate where snow grains are placed (Figure 6A). Five photographs with a macro-lens (Nikon D40) are taken successively for each illuminated direction (Figure 5B). The first photograph gives the projected area of the grain with the diode illuminating from above and the four other photographs allow the digitization of the projected shadows. Knowing the angles of illumination and the exact position of each grain on the gridded plate, it is possible to calculate the height of the grain's envelope from the tangent illumination path corresponding to the projected shadow in each direction. We thus derive a numerical height model of each snow grain and reconstruct a 3D representation of the snow grain (Figure 5B). From this elevation model, we derive multiple size parameters (values for the example shown in Figure 6A are given): projected area, mean height, maximum height, volume, total surface area, the ratio between the total surface area and the volume (noted $\text{SSA}_{\text{Shadows}}$), eccentricity, minor axis and major axis. The last three parameters are extrapolated from an ellipse enveloping the projected area of the grain. All the parameters are then averaged for each snow layer (generally about 10 grains per sample). It is clear that we cannot delimitate the cavities inside the grains, neither under the largest horizontal size. The volume and surface derived from these measurements correspond to the envelope of the snow grain and thus underestimate the true surface to volume ratio (SSA) value.

The primary interest of these macro-photographs is to better characterize the shapes of the snow grains corresponding each layer of the snowpit. Such a simple system, very easy to handle only takes few minutes to acquire the five pictures but is relatively more time consuming for their processing.

RESULTS AND DISCUSSION

Albedo vs. SSA relationship

Figure 6 shows the relationship between albedo measurements taken with the IRIS system and SSA values obtained from three different methods: 1) SWIR albedo measurements (DUFISSS) (Gallet et al., 2009), 2) methane adsorption (CH_4) (Dominé et al., 2001) and 3) X-Ray Computed Micro-Tomography (Micro-CT) (Chen and Baker, 2010). The KZ04 model was fitted on the first dataset (DUFISSS). Albedo measurements from both instruments (IRIS fixed position and DUFISSS) were taken from the same snow sample. The SSA was then derived from the DUFISSS measurements with the Gallet et al. (2009) relationship and compared to the IRIS measurements. A slight adjustment to the IRIS albedo measurements was made due to the difference in wavelength of each instrument (IRIS at 1300 nm and DUFISSS at 1310 nm) and also due to the fact that the integrating sphere of IRIS is smaller than the one used for DUFISSS (see Gallet et al., 2009). The calibration is given by:

$$R_{a,\text{DUFISSS}} = 1.024 R_{a,\text{IRIS}} + 0.025.$$

Results show a good agreement with the KZ04 model using a shape factor b of 4.29 (snow grain shape corresponding to spheres in Figure 1). Spectral albedo of snow: A) for different grain sizes (D_o) simulated with the KZ04 model for normal incident lighting ($K_0=9/7$). The spectral responses of the NIR (dark gray rectangle) and SWIR (light gray rectangle) cameras are displayed. The wavelength of the IRIS and DUFISSS laser system are included in the SWIR camera spectral response.B) ($R^2=0.99$; $\text{RMSE}=1.34 \text{ mm}^{-1}$), meaning that the snow grain shape does not scatter the points in these conditions. This calibration is limited though to samples of $\text{SSA}<50\text{mm}^{-1}$ and may differ for SSA values higher than 50mm^{-1} . The overall accuracy of the IRIS system using the KZ04 model for retrieving the SSA in comparison to all these three SSA datasets is 1.59 mm^{-1} , i.e. of the order of 10-15%.

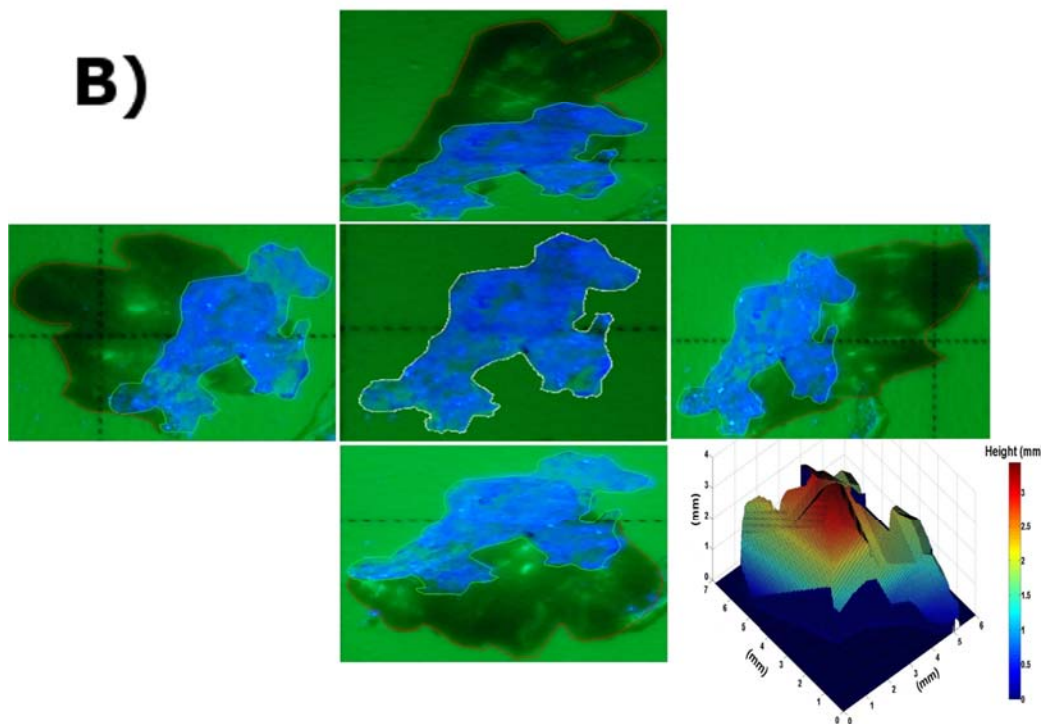
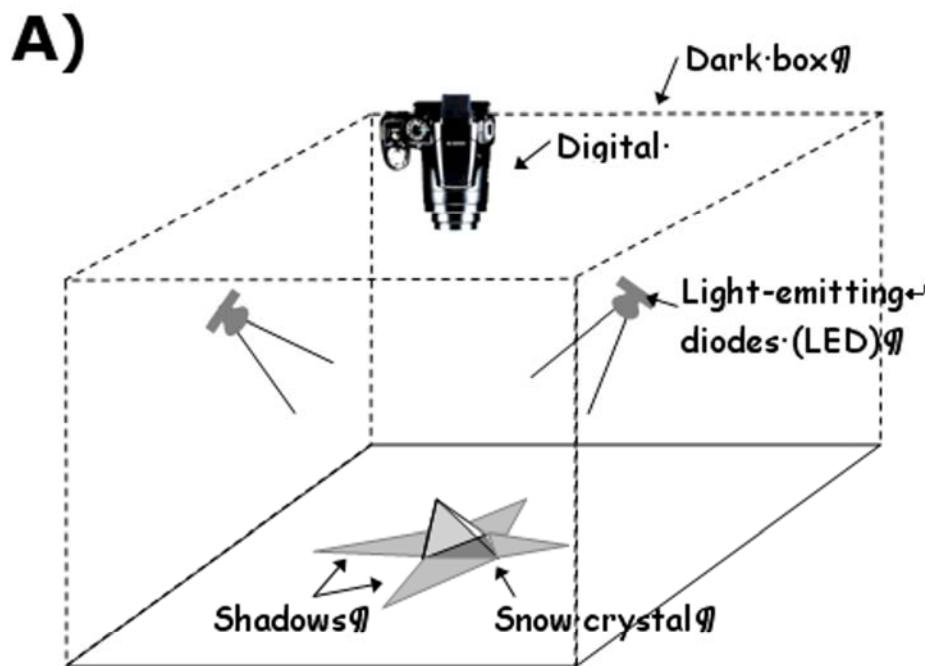


Figure 5. A) Representation of the multi-directional lighting system B) Multi-directional lighting pictures of a grain taken on the Barnes ice cap (Canada) during the 2011 winter campaign. In this case, the major axis is 7.51 mm, the minor axis is 4.05 mm and the maximum height is 3.39 mm.

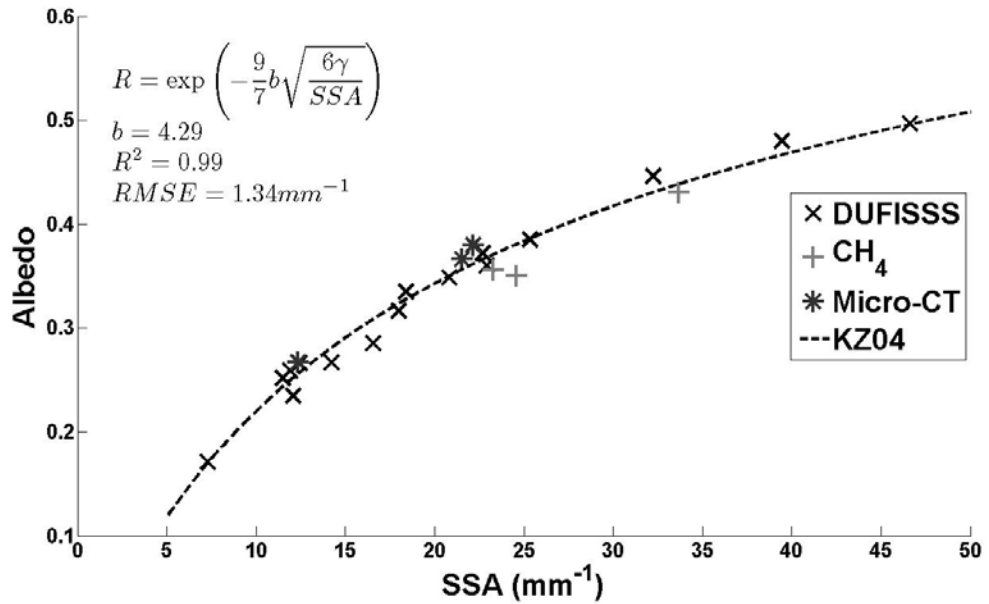


Figure 6. Relationship between the IRIS derived albedo and SSA measurements from multiple instruments.
Dotted line corresponds to the KZ04 albedo model.

SSA measurements comparisons

Figure 7 shows SSA measurements of the same snow profile taken in the French Alps with three different instruments. The first SSA profile is derived from the mobile IRIS albedo system, the second is derived from the DUFISSS system (Gallet et al., 2009) and the last one is determined by the CH₄ adsorption method.

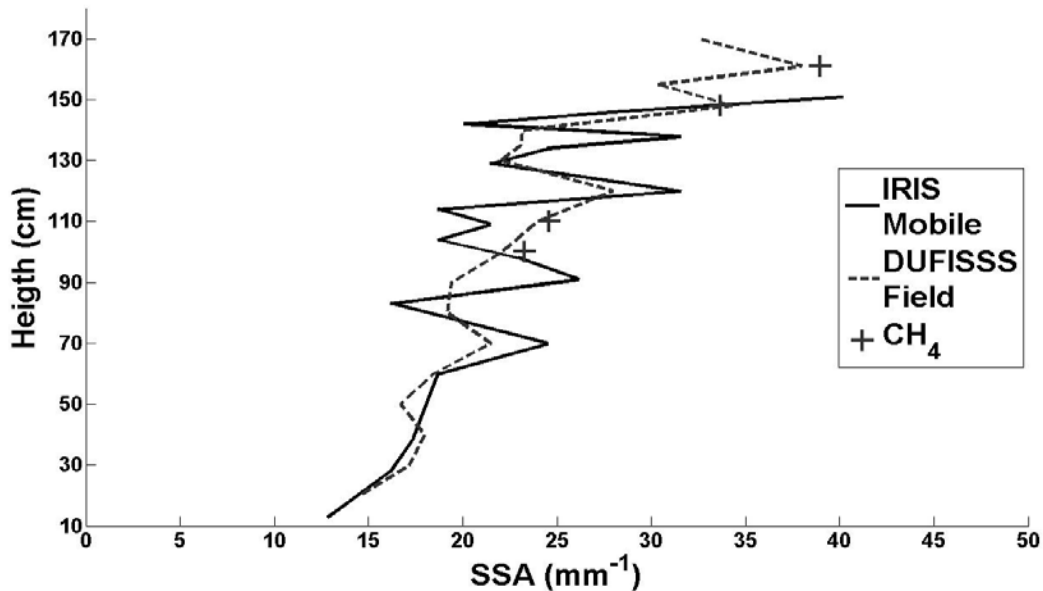


Figure 7. SSA profile derived from 3 different instruments (IRIS, DUFISS and methane adsorption) taken in the French Alps in 2009

The two SSA measurements derived from albedo profiles (IRIS and DUFISSS) are in good agreement with the methane adsorption method taken as reference even though the mobile IRIS system shows more variability. This variability may be due to the variable distance between the snow wall and the integrating sphere. The bigger the distance, the lower the reflectance as the measured energy is inversely proportional to the square of the distance between the illuminated area and the detector.

The snow SSA profile derived from the new SWIR camera system was then compared to the fixed IRIS system taken as reference. Example of measurements is shown in Figure 9 for the SIRENE site, Sherbrooke, Québec during the 2011 winter.

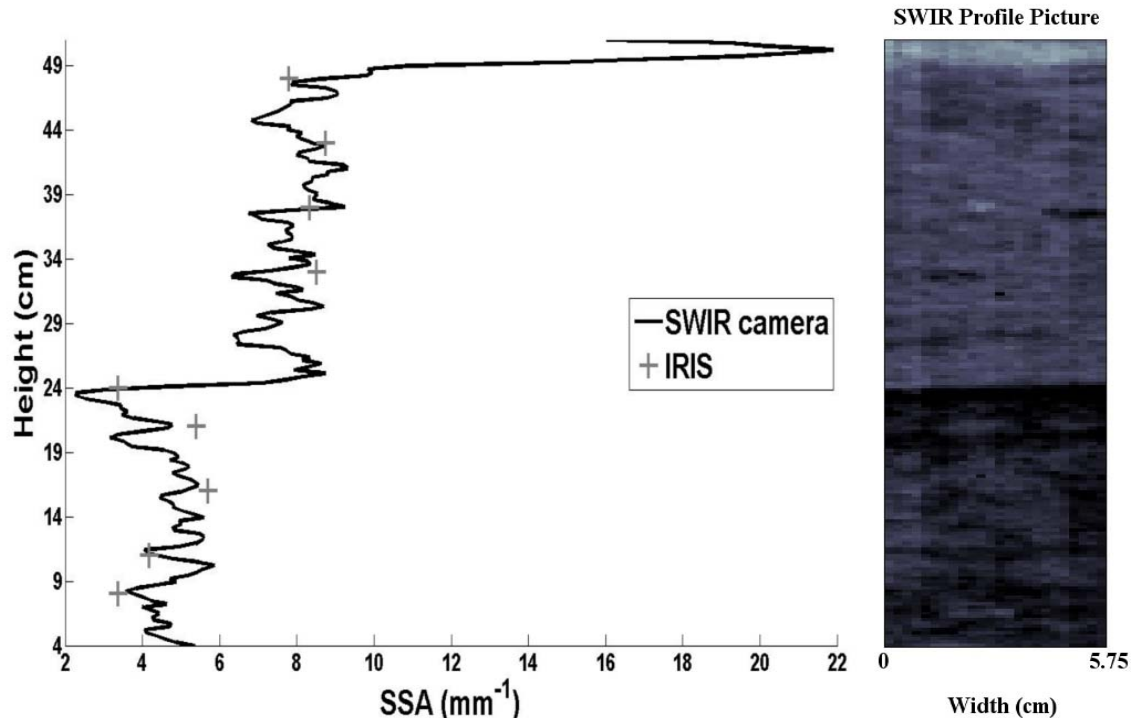


Figure 8. SSA profile derived from the fixed IRIS system (extracted samples) and the SWIR camera in Sherbrooke (Canada) during the 2011 winter. The picture on the right shows the portion of the snowpit (5.75 cm width) from which the mean SWIR albedo was computed.

The advantage of using this new SWIR camera system (other than higher sensitivity to SSA as shown in figure 1a) is that it is less sensitive to lighting conditions and camera angle. This increases the reproducibility accuracy of the measurement. But, although the SWIR camera system shows more sensitivity than the NIR camera system, there are still some issues with controlling the lighting conditions. In optimum conditions, SWIR camera measurements are in good agreement with the fixed IRIS system as shown in Figure 8 (RMSE=3.02 mm⁻¹). The optimal conditions are obtained by limiting direct illumination (on the snow wall and in the camera lens). The interest of such measurements (Figure 8) is the SSA values are provided at a 2-mm vertical resolution. With such resolution, one can clearly distinguish a fresh snow layer (49-50cm; SSA = 16.51mm⁻¹), a dense rounded snow grain slab (25-49cm; SSA=7.95 mm⁻¹) a hard snow crust (21-24cm; SSA=3.44mm⁻¹) and a coarse depth hoar layer (4-21cm; SSA=4.68mm⁻¹). The major difference between the SWIR and NIR camera measurements is the more accurate SSA values derived from the SWIR system as illustrated in Figure 9.

Figure 9 compares the NIR camera-derived SSA against the IRIS-derived SSA profile taken as reference for a subarctic snowpit at Churchill, Manitoba (Canada). In the middle, the snow SSA profile measured with the NIR camera and the fixed IRIS systems is shown with the NIR picture

corresponding to the profile on the right. The disagreements between both measurements are mainly due to the higher sensitivity to illumination conditions of the NIR camera system. At the top of the snowpit, with the higher incident light intensity on the reference panel, the albedo measured by the camera is attenuated by the albedo normalization by the reference panel. On the contrary, near the bottom of the snowpit, the incident light is less intense on the reference panel which increases the relative albedo intensity after normalization. Near the top of the snowpit, the albedo measured by the IRIS system may be too high because the wavelength used appears too short for low-density fresh snow measurements as discussed by Gallet et al. (2009).

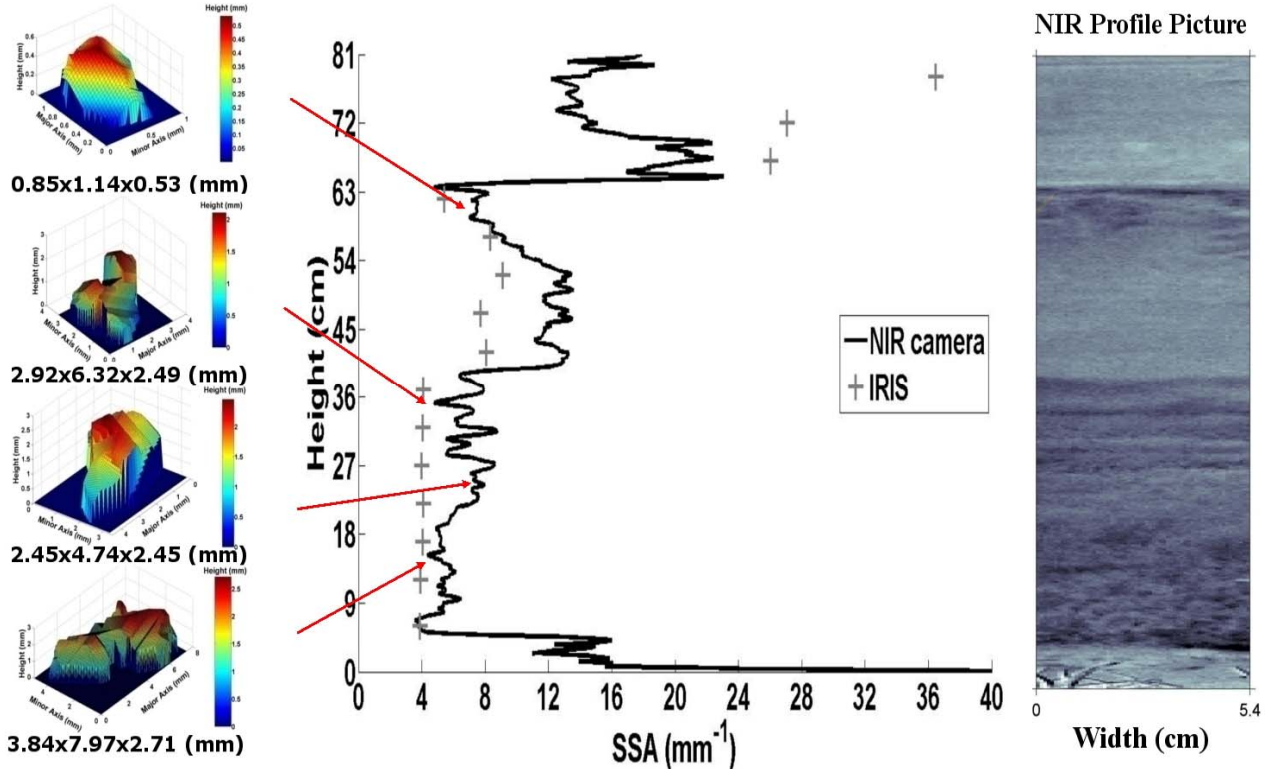


Figure 9. SSA profile derived from the IRIS and NIR camera (middle) and corresponding 3D snow grain analysis derived from the multi-directional lighting system (left) (maximum dimension are given for each selected grain). The picture on the right shows the portion of the snowpit (5.4 cm width) from which the mean NIR albedo was computed. Data are taken during the 2010 field campaign in Churchill, Manitoba (Canada)

The high vertical resolution of the NIR picture on the right of Figure 9 brings excellent visual stratigraphic information on the different snow layer. On the left side of Figure 9 examples of 3D snow grain analysis derived from the multi-directional lighting system are shown. From these measurements, we can extract grain shape information complementing the stratigraphic information of the NIR picture. The grain extension being relatively the same on the three axes for the top grain shown in Figure 9 helps to associate the grain shape of the snow layer to rounded grains. The other three grains having higher dimensions and a more elongated shape (major axis almost twice the size of the minor axis) can be associated to a depth hoar layer.

In accordance to theoretical analysis, the grain shape influences snow albedo as shown in Figure 1. Spectral albedo of snow: A) for different grain sizes (D_o) simulated with the KZ04 model for normal incident lighting ($K_0=9/7$). The spectral responses of the NIR (dark gray rectangle) and SWIR (light gray rectangle) cameras are displayed. The wavelength of the NIR and DUFISSS laser system are included in the SWIR camera spectral response.B and also discussed by Picard et al. (2009a). However, measurements do not exhibit strong variation with the type of grains.

Indeed, our measurements (Figure 6) as well as those from Gallet et al. (2009) and Arnaud et al. (2011) fit well to the KZ04 snow albedo model with a fixed shape factor value for a large variety of snow types. This means that the grain shape seems to be of second order effect on the SSA derived by optical methods. Here, the snow grain shapes were analyzed using the developed multi-directional lighting system.

Figure 10 shows the relationship, for the same snow samples, between the optical diameter (D_o) derived from the IRIS system and the longest grain extension (D_{max}) as a function of the observed maximum height estimate (H_{max}) of about 10 grains per extracted snow sample. Both parameters (D_{max} and H_{max}) were derived from the multi-directional lighting system and we considered the average value among all the grains analyzed for each sample. Figure 11 includes a large number of samples (379) covering a wide range of snow conditions along the Canadian winter from fresh snow with small grain ($D_{max} < 2\text{ mm}$) to depth hoar with very large grains ($D_{max} > 6\text{ mm}$). Layers with a low snow density were not taken into account because of the issues discussed by Gallet et al. (2009). A general trend can be seen; D_o values mostly vary between 0 - 0.9 mm while D_{max} values can vary up to 10 mm with different heights. The observed scattered clearly shows the added value of the 3D analysis. For a given D_o value, the grains can have a large range of maximum height from 1.2 to more than 2.8 mm. There are thus many grain sizes associated to a sphere having the same optical properties (D_o). This Figure obviously shows that we add more information to SSA determination with such a device. Even though the optical diameter is a more accurate parameter for snow grain size modeling, the snow grain dimensions derived from the multi-directional lighting system are still very useful for quantifying the grain type and shape, which can provide insight to the various metamorphism processes that occurred within the snowpack.

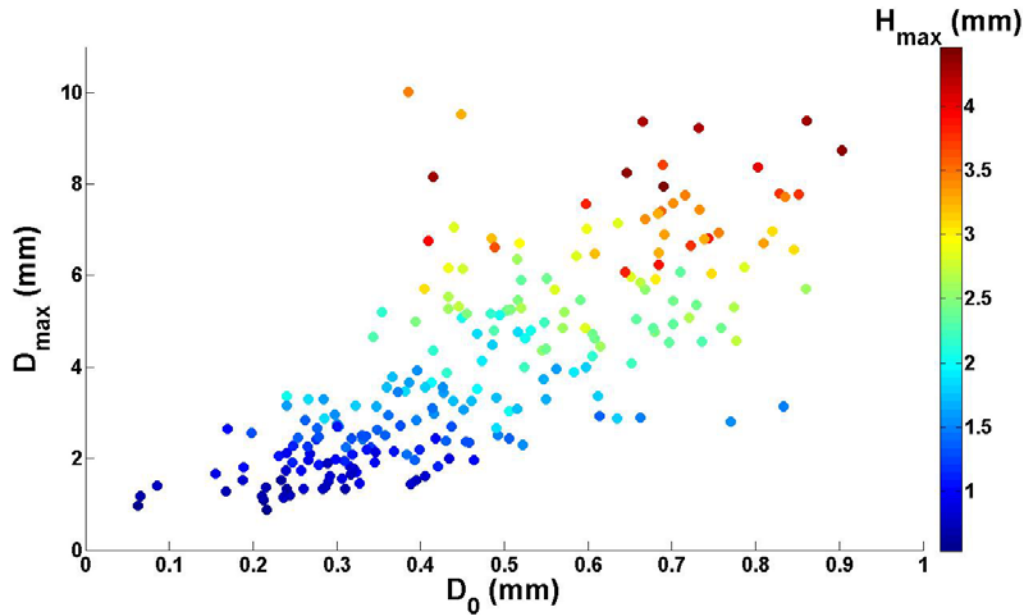


Figure 10. Comparison between geometrical (D_{max}) and optical (D_o) diameters of snow grain as a function of grain maximum height. Measurements were taken during the 2010 field campaign in Churchill, Manitoba (Canada).

CONCLUSIONS

The most accurate instrument for snow SSA determination is the IRIS system in a fixed mode (i.e. using extracted samples) which shows the best reproducibility (relative variations of 3 to 5% on SSA measurements). The mean accuracy of such a device is of the order of 10% compared to

methane adsorption method. The downside of such a system is the need to extract snow samples for measurements which can be difficult depending on snow conditions and stratigraphy (ice length, low grain cohesive layer...) and which lengthens the acquisition time to complete a full snow profile. Also, the vertical resolution of the fixed mode is lower than other systems such as the mobile IRIS system and the NIR/SWIR camera systems. The gain in vertical resolution with the mobile mode of the IRIS system reduces the accuracy of its measurements as shown in Figure 7.

The NIR camera system has shown to be less accurate for snow grain size measurement when compared to IRIS. The relative higher sensitivity to illumination conditions (Figure 9) and its low sensitivity to snow grain size variations in its spectral range (under $1\mu\text{m}$, see Figure 1A) makes this instrument less reliable for quantitative snow grain size measurements. However, its high vertical resolution ($\sim 1\text{mm}$) and its fast acquisition time (5 to 10 minutes) make it a quick and easy way to extract visual layer information characterizing the snowpack.

The lower sensitivity to illumination conditions and the higher sensitivity to the snow grain size variations (Figure 1A) make the SWIR camera a more accurate instrument for snow grain size retrieval. Although the system provides similar vertical resolution to the NIR camera ($\sim 2\text{mm}$), the SWIR camera is more complicated to install and the acquisition time is longer. However, improvements to the protocol are in progress in order to reduce the complexity of the setup and control the illumination conditions (increase the reproducibility). So far, this instrument has proven to be the best compromise between acquisition time, accuracy, reproducibility and vertical resolution.

The last instrument described in this paper is a multi-directional lighting macro-photographs system for retrieving the 3D shape of individual grain from the directional shadow size measurements. Although this system is not designed to derive SSA, the added value of the derived information on snow grain shape and type appears very valuable. The simplicity of this device and its rapid acquisition time in the field (few minutes per sample) makes the system an easy way to objectively characterize snow grain shapes and types at the different layers within the snowpack, complementarily to SSA measurements.

ACKNOWLEDGEMENTS

We thank Z. Jin who provided his albedo calculations for different grain shapes (Figure 1). Spectral albedo of snow: A) for different grain sizes (D_o) simulated with the KZ04 model for normal incident lighting ($K_0=9/7$). The spectral responses of the NIR (dark gray rectangle) and SWIR (light gray rectangle) cameras are displayed. The wavelength of the IRIS and DUFISSS laser system are included in the SWIR camera spectral response.). All the colleagues who help us during the field campaigns in France and Canada are also gratefully acknowledged. This work was supported by NSERC, Canada, the Canadian Polar Continental Shelf Program (Barnes Ice Cap field campaign), the Canadian Space Agency (Churchill field campaign, Claude Duguay and Chris Derksen P.I.), Environment Canada (Anne Walker, P.I.), CNRS France, the French Polar Institut (IPEV), the Programme international de collaboration scientifique (PICS) of CNRS, and the Ministère des Relations internationales du Québec and Ministère des Affaires étrangères et européennes de la République française (Consulat général de France à Québec) in the frame work of the 63e session de la Commission permanente de coopération franco-qubécoise.

REFERENCES

- Aoki T, Aoki T, Fukabori M, Hachikubo A, Tachibana Y, and Nishio F. 2000. Effects of snow physical parameters on spectral albedo and bidirectional reflectance of snow surface. *Journal of Geophysical Research D: Atmospheres* **105**: 10219–10236.
- Armstrong, R.L., and Brun E. 2008. *Snow and Climate: Physical Processes, Surface Energy Exchange and Modeling*. Cambridge University Press.

- Brown R. 2010. Analysis of snow cover variability and change in Québec, 1948–2005. *Hydrological Processes* **24**: 1929–1954.
- Chang A, Foster J, Hall D, Rango A, and Hartline B. 1982. Snow water equivalent estimation by microwave radiometry. *Cold Regions Science and Technology* **5**: 259–267.
- Chen S, and Baker I. 2010. Evolution of individual snowflakes during metamorphism. *Journal of Geophysical Research D: Atmospheres* **115**: 1–9.
- Derkzen C, Toose P, Rees A, Wang L, English M, Walker A, and Sturm M. 2010. Development of a tundra-specific snow water equivalent retrieval algorithm for satellite passive microwave data. *Remote Sensing of Environment* **114**: 1699–1709.
- Domine F, Albert M, Huthwelker T, Jacobi H, Kokhanovsky A A, Lehning M, and Simpson G P. 2008. Snow physics as relevant to snow photochemistry. *Atmospheric Chemistry and Physics* **8**: 171–208.
- Dominé F, Cabanes A, Taillandier A, and Legagneux L. 2001. Specific surface area of snow samples determined by CH₄ adsorption at 77 K and estimated by optical microscopy and scanning electron microscopy. *Environmental Science and Technology* **35**: 771–780.
- Durand M, Kim EJ, and Margulis SA. 2008. Quantifying uncertainty in modeling snow microwave radiance for a mountain snowpack at the Point-Scale, including stratigraphic effects. *IEEE Transactions on Geoscience and Remote Sensing* **46**(6): 1753–1767.
- Fernandes R, Zhao H, Wang X, Key J, Qu X, and Hall A. 2009. Controls on Northern Hemisphere snow albedo feedback quantified using satellite Earth observations. *Geophysical Research Letters* **36**.
- Fierz C, Armstrong RL, Durand Y, Etchevers P, Greene E, McClung DM, Nishimura K, Satyawali PK, and Sokratov SA. 2009. *The International Classification for Seasonal Snow on the Ground*. IHP-VII Technical Documents in Hydrology N°83, IACS Contribution N°1, UNESCO-IHP, Paris.
- Foster J, Hall D, Eylander J, Riggs G, Nghiem S, Tedesco M, Kim E, Montesano P, Kelly R, Casey K, and Choudhury B. 2011. A blended global snow product using visible, passive microwave and scatterometer satellite data. *International Journal of Remote Sensing* **32**: 1371–1395.
- Gallet J, Domine F, Zender C, and Picard G. 2009. Rapid and accurate measurement of the specific surface area of snow using infrared reflectance at 1310 and 1550 nm. *Cryosphere Discussions* **3**: 33–75.
- Grannas AM, Jones AE, Dibb J, Ammann M, Anastasio C, Beine HJ, Bergin M, Bottenheim J, Boxe CS, Carver G, Chen G, Crawford JH, Dominé F, Frey MM, Guzman MI, Heard DE, Helmig D, Hoffmann MR, Honrath RE, Huey LG, Hutterli M, Jacobi HW, Klan P, Lefer B, McConnell J, Plane J, Sander R, Savarino J, Shepson PB, Simpson W R, Sodeau JR, von Glasow R, Welle R, Wolff EW, and Zhu T. 2007. An overview of snow photochemistry: evidence, mechanisms and impacts. *Atmospheric Chemistry and Physics*, **7**: 4329–4373.
- Grenfell TC, and Warren SG. 1999. Representation of a nonspherical ice particle by a collection of independant spheres for scattering and absorption of radiance. *Journal of Geophysical Research* **104**(31): 697–31,709.
- Hall A. 2004. The role of surface albedo feedback in climate. *Journal of Climate* **17**: 1550–1568.
- Jin Z, Charlock TP, Yang P, Xie Y, and Miller W. 2008. Snow optical properties for different particle shapes with application to snow grain size retrieval and MODIS/CERES radiance comparison over Antarctica. *Remote Sensing of Environment* **112**: 3563–3581.
- Kokhanovsky AA, and Zege EP. 2004. Scattering optics of snow. *Applied Optics* **43**: 1589–1602.
- Langlois A, Royer A, and Goïta K. 2010a. Analysis of simulated and spaceborne passive microwave brightness temperatures using in situ measurements of snow and vegetation properties. *Canadian Journal of Remote Sensing* **36**: S135–S148.
- Langlois A, Royer A, Montpetit B, Picard G, Brucker L, Arnaud L, Harvey-Collard P, Fily M, and Goïta K. 2010b. On the relationship between snow grain morphology and in-situ near infrared calibrated reflectance photographs. *Cold Regions Science and Technology* **61**: 34–42.
- Lyapustin A, Tedesco M, Wang Y, Aoki T, Hori M, and Kokhanovsky A. 2009. Retrieval of snow grain size over Greenland from MODIS. *Remote Sensing of Environment* **113**(9): 1976–1987.

- Matzl M, and Schneebeli M. 2006. Measuring specific surface area of snow by near-infrared photography. *Journal of Glaciology* **52**: 558–564.
- Matzl M, and Schneebeli M. 2010. Stereological measurement of the specific surface area of seasonal snow types: Comparison to other methods, and implications for mm-scale vertical profiling. *Cold Regions Science and Technology* **64** (2010) 1–8.
- Mätzler C. 2002. Relation between grain-size and correlation length of snow. *Journal of Glaciology* **48**: 461–466.
- Mätzler C. 2006. Thermal microwave radiation - applications for remote sensing. *IEE Electromagnetic Waves Series, Institution of Electrical Engineers (IEE), London, U.K.*
- Picard G, Arnaud L, Domine F, and Fily M. 2009a. Determining snow specific surface area from near-infrared reflectance measurements: Numerical study of the influence of grain shape. *Cold Regions Science and Technology* **56**: 10–17.
- Picard G, Domine F, Arnaud L, Champollion N, Cliche P, Dufour A, Flin F, Gallet J, Langlois A, Lesaffre B, and Royer A. 2009b. Comparison of six experimental methods to measure snow SSA in the field. *Eos Trans. AGU, 90(52), Fall Meet. Suppl.*, Abstract C41D-08.
- Pulliainen J. 2006. Mapping of snow water equivalent and snow depth in boreal and sub-arctic zones by assimilating space-borne microwave radiometer data and ground-based observations. *Remote Sensing of Environment* **101**: 257–269.
- Taillardier A, Domine F, Simpson W, Sturm M, and Douglas T. 2007. Rate of decrease of the specific surface area of dry snow: Isothermal and temperature gradient conditions. *Journal of Geophysical Research F: Earth Surface*, **112**.
- WiscombeWJ. 2005. Refractive indices of ice and water.
(<ftp://climate1.gsfc.nasa.gov/wiscombe/>).
- Yang P, and Liou K. 1996. Geometric-optics-integral-equation method for light scattering by nonspherical ice crystals. *Applied Optics*, **35**: 6568–6584.